nature communications

Article

https://doi.org/10.1038/s41467-025-65074-7

# Cu/Zn/histidine supramolecular assemblies with optimized Cu catalytic sites as an alternative of superoxide dismutase

Received: 19 February 2025

Accepted: 7 October 2025

Published online: 18 November 2025

Check for updates

Hao Jin[1,2], Xuanqi Zhu[1,2], Mengsi Zhang[2], Hao Zheng[1], Yang Chen[1], Dong Yao[3], Shuwei Liu[2] ✉ & Hao Zhang[1,2] ✉

Superoxide dismutase (SOD), featured with unique metal catalytic sites, is the first defense against reactive oxygen species (ROS) damage in vivo and well used in the treatment of oxidative stress-related diseases. However, the catalytic activity of natural SOD is limited by the metal ion coordination with rigid amino-acid residues. Inspired by the $Cu^{2+}$/histidine residue coordination in Cu-Zn-SOD, in this work, the Gibbs free energy change of the break/reform of coordination bonds in the tetracoordinated structure formed by $Cu^{2+}$ and different groups in histidine is calculated, which reveals that in comparison to the Cu catalytic site coordinated with four imidazolyls, the coordination with one amino, one carboxyl and two imidazolyls possesses the lowest overall energy as well as the lowest breaking energy of one of the coordination bonds. Thus, catalytic site stability and catalytic reaction activity can be balanced sufficiently. Accordingly, the as-prepared Cu/Zn/histidine (CuZnHis) supramolecular assemblies with optimized Cu catalytic site present a significantly enhanced SOD activity up to 37900 Unit/mg, which is at least 5.4 times higher than that of natural Cu-Zn-SOD. As a proof of concept in treating oxidative stress-related diseases, the CuZnHis assemblies promote macrophage polarization from M1 to M2 phenotype and the expression of anti-inflammatory factors, and inhibit the periodontitis in male animal models.

Redox homeostasis of the cells is the basis for maintaining normal life activities, which is fundamentally achieved by the net physiological balance of intracellular redox reactions[1–3]. The imbalance of intracellular redox, typically the increase of reactive oxygen species (ROS) level, may cause more than 200 oxidative stress-related diseases, such as rheumatoid arthritis[4], atherosclerosis[5], periodontitis[6], and so on[7,8]. As the first defense against ROS damage, superoxide dismutase (SOD) can effectively eliminate superoxide anion ($O_2^{\cdot-}$) and reduce oxidative stress by virtue of its unique catalytic site formed by the coordination of metal ions and amino-acid residues[9–11]. With respect to metal prothetic groups, the most frequent types of SOD include Cu-Zn-SOD and Mn-SOD[12,13]. For Cu-Zn-SOD, the catalytic site is the tetracoordinate structure of copper ion ($Cu^{2+}$) with four imidazolyls of histidine residues[14–16], and the coordinated zinc ion ($Zn^{2+}$) plays the role in maintaining structural integrity[17–19]. For Mn-SOD, the catalytic site is the tetracoordinate structure of manganese ion ($Mn^{2+}$) with three imidazolyls of histidine residues and one carboxyl of aspartic acid residue[11,20]. Despite the catalytic sites of natural SOD are clear, the catalytic activity is generally limited in 2500-7000 Unit/mg, which is not fully satisfactory for more extensive applications.

Taking mostly used Cu-Zn-SOD as the example, in the catalytic reaction, the coordinated $Cu^{2+}$ reacts with one $O_2^{\cdot-}$ to form cuprous ion

[1]State Key Laboratory of Supramolecular Structure and Materials, College of Chemistry, Jilin University, Changchun, P. R. China. [2]Institute of Translational Medicine, The First Hospital of Jilin University, Changchun, P. R. China. [3]Institute of Theoretical Chemistry, College of Chemistry, Jilin University, Changchun, P. R. China. ✉e-mail: liushuwei@jlu.edu.cn; hao_zhang@jlu.edu.cn

($Cu^+$) and oxygen ($O_2$), and subsequently, $Cu^+$ and another $O_2^{\cdot-}$ generate $Cu^{2+}$ and hydrogen peroxide ($H_2O_2$) in the presence of hydrogen ion ($H^+$) to finish a catalytic cycle and present SOD activity[14,15,21,22]. This process is accompanied by the break/reform of the coordination bond between $Cu^{2+}$ and one of the imidazolyls, leading to the redox reaction of $Cu^{2+}$ with electron gain or loss[15,16,23,24]. However, the simultaneous coordination of $Cu^{2+}$ with four imidazolyls generates severe steric hindrance[25]. On the one aspect, this is unfavorable to the binding of catalytic sites and reactants, thus reducing the efficiency of catalytic reaction[26,27]. On the other aspect, the overall energy of the catalytic site is high, which reduces the stability. In addition, the energy required to break the $Cu^{2+}$/imidazolyl coordination bond is not the lowest in comparison to $Cu^{2+}$/carboxyl and $Cu^{2+}$/amino coordination, leading to a negative impact on the catalytic activity also[28,29]. In view of these problems, targeted optimization of the catalytic site of Cu-Zn-SOD is promising for enhancing the activity of SOD.

As mentioned above, the rigid $Cu^{2+}$/imidazolyl coordination may be the key that limits the activity of Cu-Zn-SOD. To optimize Cu catalytic site, it is necessary to reduce the overall energy of $Cu^{2+}$ coordination environment and particularly the energy required to break one of the $Cu^{2+}$-related coordination bond[30,31]. Inspired by Mn-SOD with both $Mn^{2+}$/imidazolyl and $Mn^{2+}$/carboxyl coordination, additional groups may also participate in the Cu catalytic site of SOD, which is expected to combine the advantage of both Cu-Zn-SOD and Mn-SOD[32]. In this scenario, molecular histidine instead of histidine residue may introduce additional $Cu^{2+}$/carboxyl and $Cu^{2+}$/amino coordination, which is considered as an alternative in catalytic site optimization[33–35]. Operationally, supramolecular assembly is capable of constructing innovative nanomaterials with the compatibility of structural integrity and dynamic binding, which is potential for designing artificial SOD with improved catalytic activity[36,37]. In existing studies, metal ion/amino-acid coordination has been employed to build supramolecular nanomaterials towards artificial SOD[38–40]. Although the catalytic function has been verified, the catalytic activity is still at relatively low level. The main limitations are attributed to the differences of natural SOD and artificial ones in the species of amino-acid ligands and the lack in regulating coordination conformation, which are the keys for optimizing Cu catalytic site and enhancing catalytic activity.

In this work, by estimating the Gibbs free energy change ($\Delta G$) of the break/reform of $Cu^{2+}$/histidine coordination with different manner, a Cu catalytic site with optimized coordination environment of one amino, one carboxyl and two imidazolyls is proposed. This optimized Cu catalytic site is further achieved by regulating the entropy-driven formation process of Cu/Zn/histidine (CuZnHis) supramolecular assemblies. In comparison with the $Cu^{2+}$/imidazolyl bond of natural SOD, the break/reform of $Cu^{2+}$/amino bond of CuZnHis assemblies exhibits lower energy, thus significantly enhances catalytic activity. The CuZnHis assemblies present the SOD activity as high as 37900 Unit/mg, which is at least 5.4 times higher than that of natural Cu-Zn-SOD and also one of the best in existing artificial SODs[41–47]. As a proof of concept in treating oxidative stress-related diseases, the CuZnHis assemblies can promote the macrophage polarization from M1 to M2 phenotype and the expression of anti-inflammatory factors, and inhibit the periodontitis in male animal models (Fig. 1).

## Results and Discussion

To optimize the Cu catalytic site based on $Cu^{2+}$ and histidine, the coordination modes of them are considered first. Starting from the tetracoordinate structure of $Cu^{2+}$ with the imidazolyls in histidine residues of natural Cu-Zn-SOD, the influence of binding site of histidine on the stability and catalytic activity of Cu catalytic site is systematically investigated. For convenience, the coordination of $Cu^{2+}$ with four imidazolyls is defined as Structure A (Fig. 2a), with one amino and three imidazolyls is defined as Structure B (Fig. 2b), with one carboxyl and three imidazolyls is defined as Structure C (Fig. 2c). While the coordination of $Cu^{2+}$ with one amino, one carboxyl and two imidazolyls is defined as Structure D (Fig. 2d). By calculating the $\Delta G$ in the transformation from Structure A to B, C, and D, the thermodynamic stability of the above four structures is determined. Since reduced energy indicates the increase of thermodynamic stability, the order of structure stability should follow the sequence of Structure D, C, A and B (Fig. 2). In general, amino coordination declines structure stability, and carboxyl coordination enhances structure stability. The reason is attributed to the steric hindrance of coordination structure and the length of coordination bond. Although the steric hindrance of amino is small, the bond length of $Cu^{2+}$/amino coordination is longer than that of $Cu^{2+}$/imidazolyl coordination, resulting in the worse stability of Structure B. The $Cu^{2+}$/carboxyl coordination processes both lower steric hindrance and shorter bond length than that of $Cu^{2+}$/imidazolyl coordination, which improves the stability of Structure C. Note that $Cu^{2+}$/amino coordination and $Cu^{2+}$/carboxyl coordination coexist in Structure D. On the one hand, the significant reduction of steric hindrance not only improves the stability of Cu catalytic sites but also strengthens the contact of catalytic sites and reactants. On the other hand, the relative instability of $Cu^{2+}$/amino coordination gives the chance for improving catalytic activity.

The catalytic activity depends on the break/reform of one of the coordination bonds in the Cu catalytic site, which leads to the redox reaction of $Cu^{2+}$ with electronic gain or loss. Since the coordinative environment of Cu catalytic site of the four structures is different, the broken/reformed bond is determined first. Considering the catalytic principle of Cu-based SOD, the coordinative group with stronger protonation ability is more likely to participate in the catalytic reaction. So, $Cu^{2+}$/imidazolyl coordination should be involved for Structure A, $Cu^{2+}$/amino coordination for Structure B and D, and $Cu^{2+}$/carboxyl coordination for Structure C. Because the $\Delta G$ of reaction mainly relates to enthalpy, entropy and temperature, the difference in the structure of Cu catalytic site will not cause a significant difference in the overall $\Delta G$ of catalytic reaction, which is supported by the calculated results in Fig. 3. However, from the viewpoint of initiating reaction, the catalytic activity should be determined by the breaking of $Cu^{2+}$ coordination bond mainly. For Structure A, the calculated $\Delta G$ of the first two steps associated with the breaking of $Cu^{2+}$/imidazolyl bond is −11.55 kcal/mol (Fig. 3a). And the $\Delta G$ associated with $Cu^{2+}$/amino bond breaking in Structure B is −10.62 kcal/mol (Fig. 3b). For $Cu^{2+}$/carboxyl bond breaking in Structure C, the $\Delta G$ is −10.68 kcal/mol (Fig. 3c). The calculated results reveal that the Cu catalytic sites of the above three structures almost possess the same ability to initiate catalytic reactions. In comparison, the $\Delta G$ of the first two steps for Structure D reaches −21.46 kcal/mol (Fig. 3d), which means that $Cu^{2+}$/amino bond breaking is easier to occur spontaneously, thus improving the catalytic activity potentially. Compared with the natural Cu-Zn-SOD catalytic site of one $Cu^{2+}$ with four imidazolyls, the coordination of $Cu^{2+}$ with one amino, one carboxyl, and two imidazolyls may act as an optimized catalytic site. This catalytic site is helpful to maintain structural stability, reduce steric hindrance, enhance the contact with reactants, reduce the energy to initiate catalytic reaction, and therewith improve the catalytic activity.

Accordingly, CuZnHis(L) supramolecular assemblies are prepared through an entropy-driven self-assembly of $Cu^{2+}$, $Zn^{2+}$, and L-histidine. The so-called entropy-driven self-assembly refers to the regulated self-assembly of components by enhancing the total entropy of system[48]. In the experiments, acetone is introduced into the aqueous solution to increase the mixing entropy of the blending system significantly, which weakens the dependence of assembly process on specific interactions and permits to regulate the assembly structure dynamically[49]. The as-prepared CuZnHis(L) assemblies present an average diameter of 264 nm under transmission electron microscopy (TEM), a hydrated diameter of 474 nm, and a surface potential of +56.8 mV (Fig. 4a, b). Although CuHis(L) assemblies are also prepared

https://doi.org/10.1038/s41467-025-65074-7

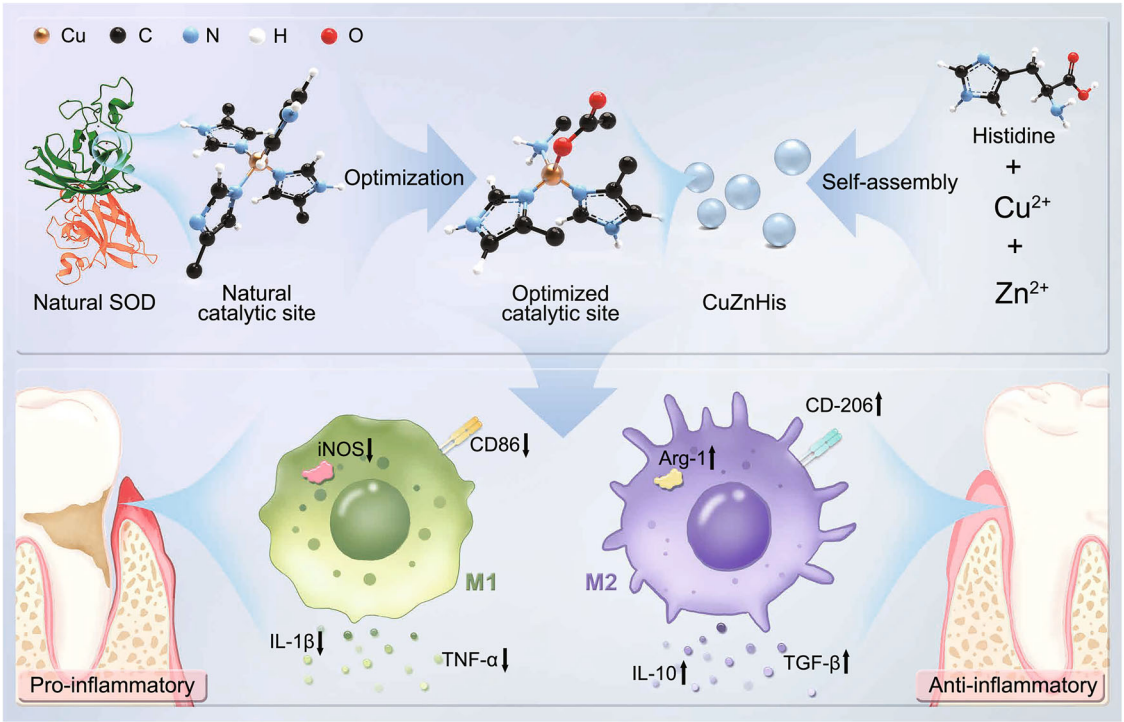


**Fig. 1 | Schematic illustration of the work.** Top: the optimization of Cu catalytic site and preparation of CuZnHis assemblies with optimized catalytic site. Bottom: the anti-inflammatory mechanism.

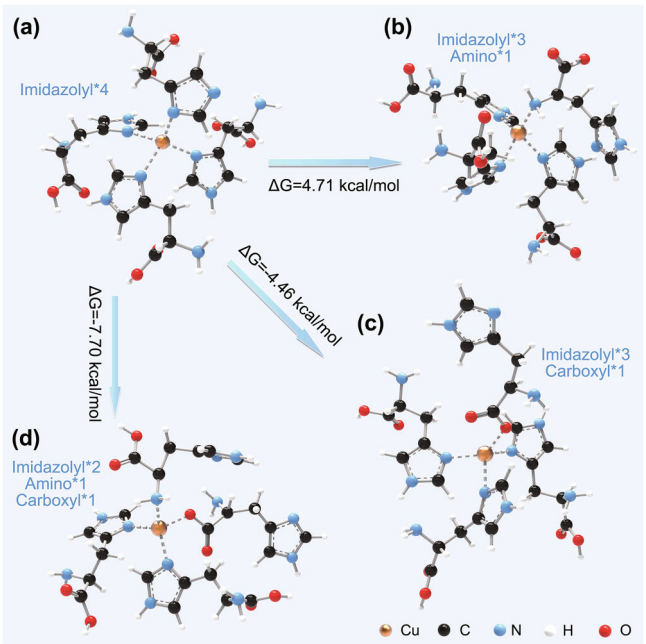


**Fig. 2 | Comparison of the thermodynamic stability of Cu catalytic sites with different structures. a** $Cu^{2+}$ coordinates with four imidazolyls. **b** $Cu^{2+}$ coordinates with one amino and three imidazolyls. **c** $Cu^{2+}$ coordinates with one carboxyl and three imidazolyls. **d** $Cu^{2+}$ coordinates with one amino, one carboxyl and two imidazolyls.

in the absence of $Zn^{2+}$, their TEM size is 429 nm, which is much higher than that of CuZnHis(L) assemblies (Fig. S1). This indicates the effect of $Zn^{2+}$ on reducing the size of assemblies. The characteristic peaks of CuZnHis(L) assemblies at 1628 and 1703 $cm^{-1}$ in the Fourier transform infrared (FTIR) spectrum are assigned to the stretching vibration of carbonyl group, the peak at 2914 $cm^{-1}$ is attributed to the stretching vibration of C-H, and the peak at 3312 $cm^{-1}$ is attributed to the stretching vibration of N-H (Fig. 4c). In addition, the characteristic peaks at 1356 and 1524 $cm^{-1}$ in the Raman spectrum originate from the imidazole ring structure (Fig. S2). By combining the data of FTIR and Raman spectra, the existence of histidine in CuZnHis(L) assemblies is proved. In element mapping detection, C, O and N signals, the main elements of histidine, are strong. Meanwhile, strong Cu and weak Zn signals are also displayed, which not only proves the existence of metal ions, but also indicates the relative contents (Fig. S3). The thermogravimetry-mass spectrometry (TG-MS) data under an air atmosphere show that CuZnHis(L) assemblies lose free and bound water in their structure first. Then, histidine begins thermal decomposition at 155 °C and completes at 530 °C. The remains are CuO and ZnO (Figs. 4d, S4). Further combined with the contents of Cu and Zn measured by inductively coupled plasma-atomic emission spectrometry (ICP-AES), the mass fraction of each component in CuZnHis(L) assemblies is estimated as 19.1%, 0.6%, 70.4% and 9.9% for Cu, Zn, L-histidine, and water, respectively.

Then the structure of CuZnHis(L) assemblies is further characterized. On the whole, the XRD pattern of the assemblies does not show diffraction peaks, implying an amorphous structure without cupric oxides or cupric hydroxides (Fig. S5). Matrix-assisted laser desorption/ionization time of flight mass spectrometry (MALDI-TOF MS) demonstrates that the fragments of assemblies possess Cu/histidine coordination structure (Fig. 4e). So, the coordinative environment of copper ions is studied by X-ray photoelectron spectroscopy (XPS). The Cu 2*p* characteristic peaks and Auger spectrum prove that the valence of Cu is +2 (Figs. S6, S7). Further analysis reveals that the ratio of amino, carboxyl, and imidazolyl coordinated with $Cu^{2+}$ is close to 1:1:2 according to the ratio of peak area (Fig. 4f). The valence and coordination environment of copper ions are further confirmed by synchrotron radiation photoelectron spectroscopy. The absorption edge of CuZnHis(L) assemblies is near CuO, indicating that the average valence of copper ions is +2 (Fig. 4g). According to the fitting of extended X-ray absorption fine structure spectra (EXAFS), $Cu^{2+}$ has a

https://doi.org/10.1038/s41467-025-65074-7

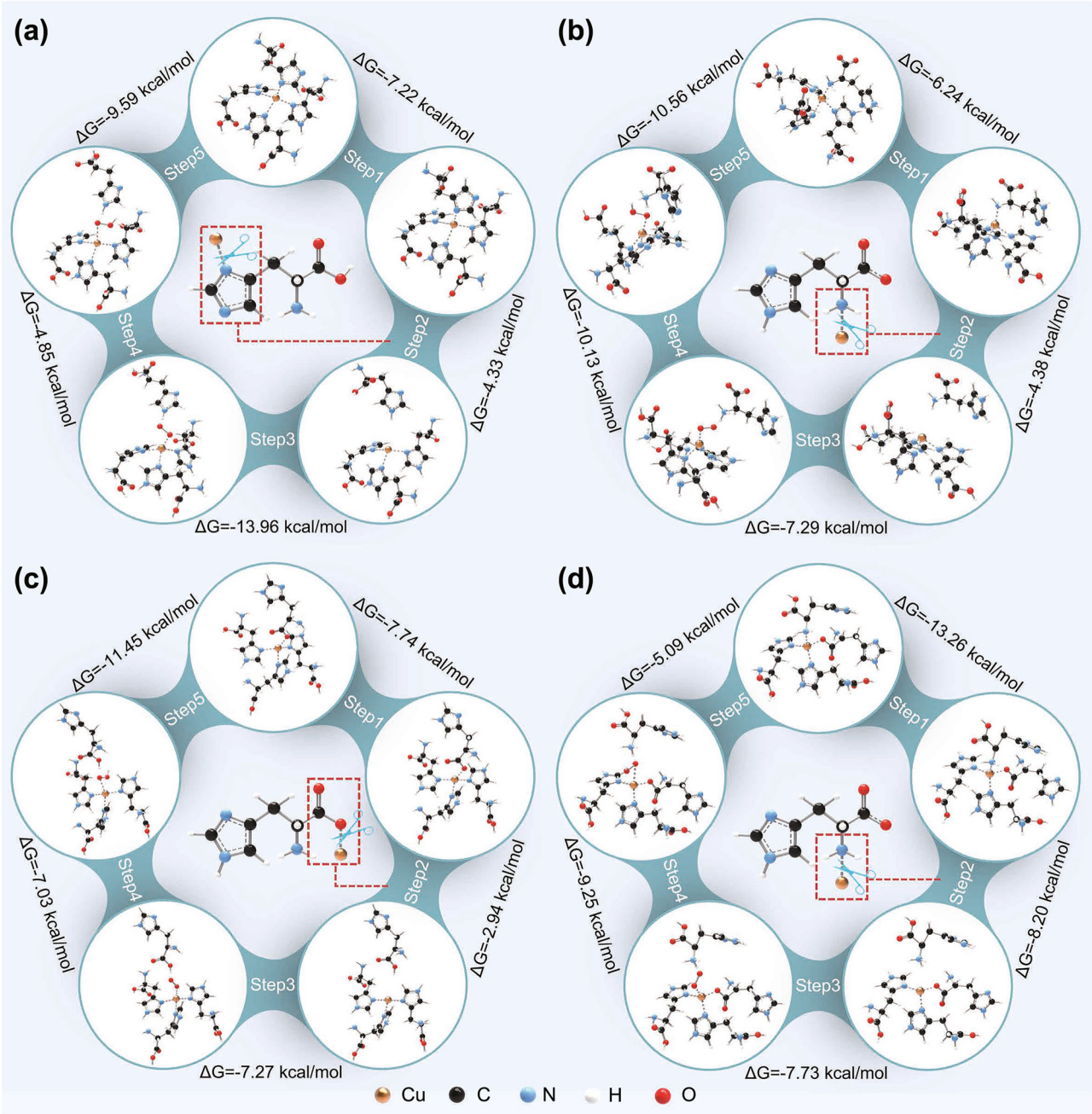


**Fig. 3 | Comparison of the Δ*G* of each step of the reaction catalyzed by Cu sites with different structures.** **a** $Cu^{2+}$ coordinates with four imidazolyls. **b** $Cu^{2+}$ coordinates with one amino and three imidazolyls. **c** $Cu^{2+}$ coordinates with one carboxyl and three imidazolyls. **d** $Cu^{2+}$ coordinates with one amino, one carboxyl and two imidazolyls.

tetracoordinate structure. There are three Cu-N bonds and one Cu-O bond around $Cu^{2+}$ (Table S1, Fig. 4h, i). Therefore, the coordination site of $Cu^{2+}$ with one amino (Cu-N), one carboxyl (Cu-O), and two imidazolyls (Cu-N) is verified (Fig. 4i illustration).

As mentioned above, the formation of CuZnHis(L) supramolecular assemblies involves an entropy-driven self-assembly process, because the sum of intermolecular weak interactions makes the influence of system entropy prominent. Regarding the self-assembly driving forces, the structure of CuZnHis(L) assemblies can be seriously damaged by EDTA, DMSO, and Tween-20 solutions, indicating that the driving forces mainly include coordination, π-π, and hydrophobic interactions (Fig. S8a–c). While urea and NaCl have no significant influence on the structure of assemblies, excluding the driving forces of hydrogen bonding and electrostatic interaction (Fig. S8d, e). Note that EDTA, DMSO, and Tween-20 do not exist in vivo, so their damage to the assemblies does not raise doubt on biological stability. Regulation of self-assembly is embodied in three aspects. The first aspect is the regulation of pH. The influence of pH on entropy is relatively small, mainly affecting the coordination of metal ions and histidine. The mixed solution containing $Cu^{2+}$, $Zn^{2+}$, and L-histidine presents strong acidity at room temperature, so that the coordination of $Cu^{2+}$ and imidazolyl in L-histidine is dominant on account of the protonation of the amino and the inhibition of carboxyl ionization. Under this condition, no product is generated in the mixed solution (Fig. S9). Then the pH adjustment by adding NaOH in the solution promotes the deprotonation of $-NH_3^+$ and the formation of $-COO^-$, thereby facilitating the $Cu^{2+}$/amino and $Cu^{2+}$/carboxyl coordination. But the increase of pH has no obvious effect on the entropy, and there is still no product generated at room temperature (Fig. S10). Thus, the regulation of temperature is performed as the second aspect. The influence of

https://doi.org/10.1038/s41467-025-65074-7

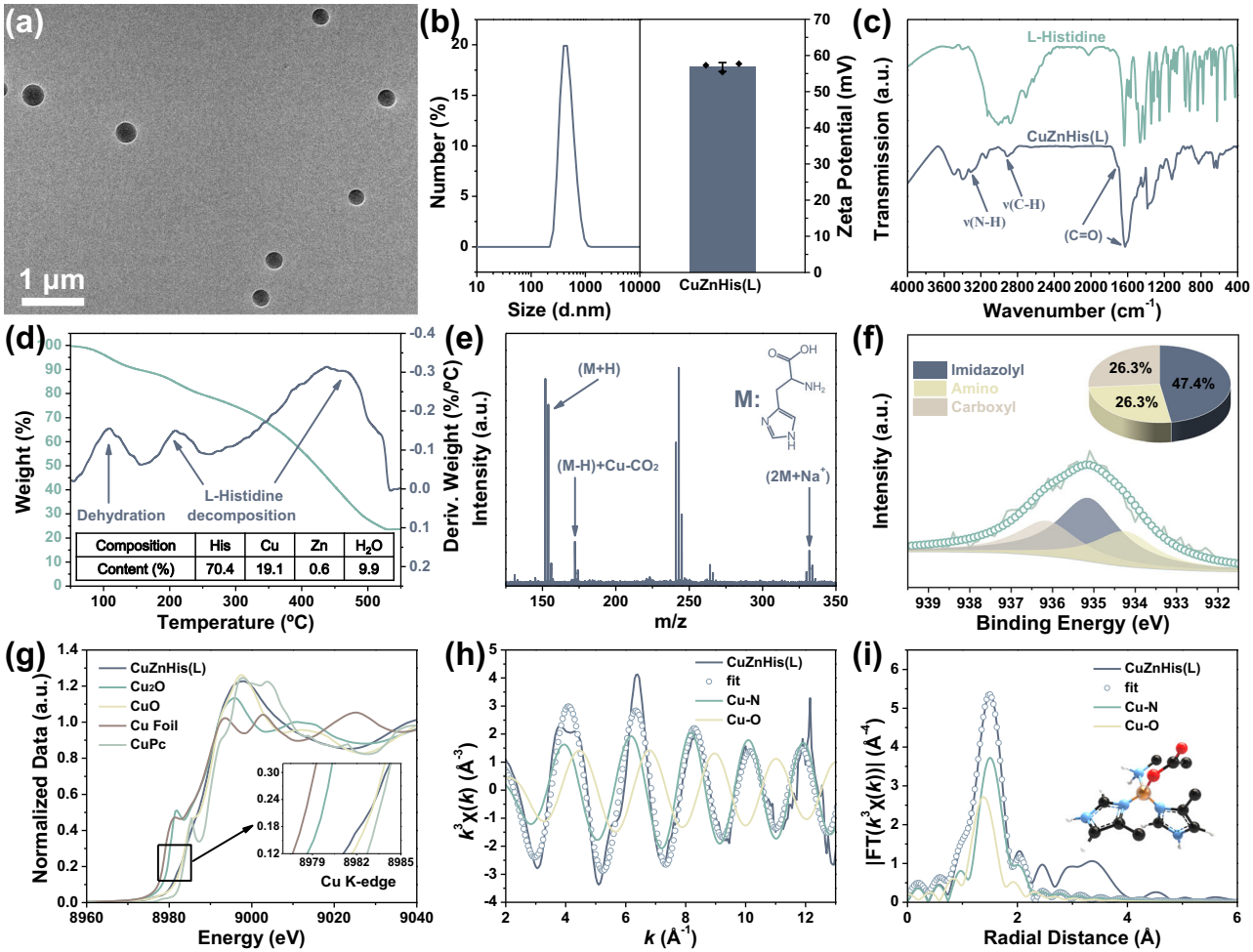


**Fig. 4 | Characterization of the morphology, composition and structure of CuZnHis(L) assemblies. a** The average diameter in TEM images was 264 nm ($n = 50$ nanoparticles). **b** Hydrated diameter and zeta potential. Zeta potential are presented as mean ± SD ($n = 3$). **c** FTIR spectra. **d** TGA and DTG analysis. **e** MALDI-TOF mass spectrum. **f** XPS Cu $2p_{3/2}$ spectrum. **g** XANES spectra at the Cu K-edge. **h**, **i** EXAFS fitting curves of Cu in CuZnHis(L).

temperature on entropy is manifested more directly. Based on pH adjustment, the increased reaction temperature at 50 °C greatly accelerates the reaction rate and the generation of products, though the morphology of the products is irregular (Fig. S11). The increase in entropy caused by the rise in reaction temperature does indeed drive the self-assembly process, but the regularity of the products still needs to be improved. The above results highlight the importance of the system entropy influenced by solvent composition as the third aspect of regulation. The addition of acetone significantly increases the total entropy of the system, and the morphology of the products becomes regular gradually. The optimum acetone-to-water volume ratio is 2:1, at which point the products with spherical morphology are generated (Fig. S12). This means that the entropy increase of the mixed solvents compared to single solvent does indeed drive the self-assembly. However, when the ratio of acetone further rises to 4:1, insoluble histidine is clearly observed in the system, because the self-assembly is suppressed due to the poor solubility of histidine (Fig. S13). The assembly process is monitored by low-temperature electron paramagnetic resonance (EPR) spectra. The continuous shift of EPR peak reflects the variation of the coordinative environment of $Cu^{2+}$ during the assembly (Fig. S14). In addition, the pH of the solution does not change significantly with the extension of reaction duration, indicating no obvious hydrolysis of $Cu^{2+}$ (Fig. S15). These results support the gradual and partial replacement of $Cu^{2+}$/imidazolyl bond by $Cu^{2+}$/carboxyl and $Cu^{2+}$/amino bond via entropy-driven process. Methanol, ethanol and DMSO are also employed to regulate the assembly process, but the effect is worse than acetone (Fig. S16). Furthermore, L-histidine is replaced by D-histidine for the preparation. The as-prepared CuZnHis(D) assemblies indicate similar morphology and size to CuZnHis(L), except the opposite chirality (Fig. S17).

CuZnHis(L) assemblies with optimized Cu catalytic site exhibit enhanced SOD activity. As shown in Fig. 5a, the assemblies are capable of scavenging $O_2^{\cdot-}$ with the clearance rate close to 100% at a very low dose of 1 μg/mL. The removal ability of the assemblies on $O_2^{\cdot-}$ is further proved by the EPR spectra (Fig. 5b). Significantly, the IC50 value and specific activity of CuZnHis(L) assemblies are 0.132 μg/mL and 37900 Unit/mg, respectively, measured by WST-8 method. In comparison, the IC50 value and specific activity of natural SOD measured under the same conditions are only 0.738 μg/mL and 6800 Unit/mg (Fig. S18). The measured activity of natural SOD consists with the reported activity generally concentrated in 2500-7000 Unit/mg[50]. It means that the SOD activity of CuZnHis(L) assemblies is at least 5.4 times higher than that of natural SOD. Even in the comparison with other artificial SODs in the ever-reported works, the SOD activity of CuZnHis(L) assemblies is also far ahead[41–47]. As shown in Table S2, the activity of CuZnHis(L) assemblies is much higher than that of common nanoenzymes, such as cerium oxide nanoenzyme and platinum-based nanoenzyme[41,51], also being 1.7 times of the single-atom nanoenzyme with the highest SOD activity reported[43]. In addition, the IC50 value and specific activity of CuHis(L) assemblies without coordinated $Zn^{2+}$ are 0.339 μg/mL and 14700 Unit/mg, respectively (Fig. S19). The difference in specific activity between CuZnHis(L) and CuHis(L)

https://doi.org/10.1038/s41467-025-65074-7

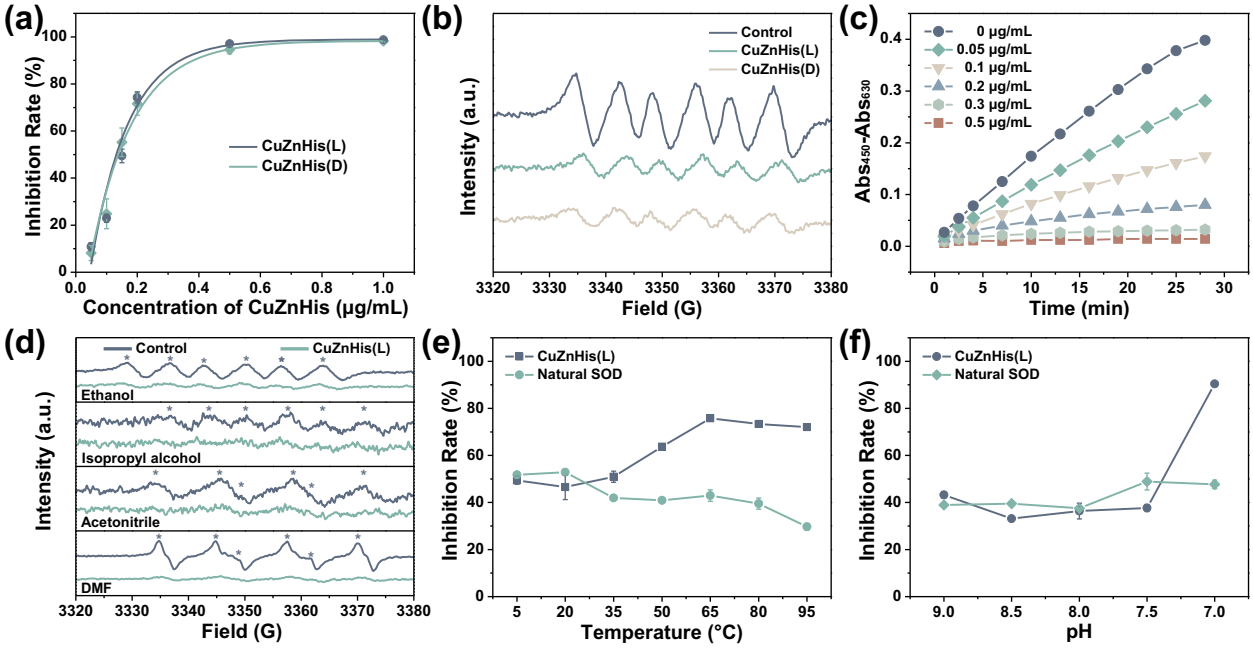


**Fig. 5 | Characterization of the SOD activity of CuZnHis assemblies. a** The specific activity graph of CuZnHis(L) and CuZnHis(D) according to the scavenging of $O_2^{\cdot-}$. **b** EPR spectra for the evaluation of $O_2^{\cdot-}$ scavenging ability of CuZnHis(L) and CuZnHis(D). **c** Time-dependent absorbance changes with different concentrations of CuZnHis(L). Smaller difference means stronger $O_2^{\cdot-}$ scavenging ability. **d** EPR spectra for the evaluation of $O_2^{\cdot-}$ scavenging ability of CuZnHis(L) in different solvents. **e** Comparison of SOD activity between CuZnHis(L) and natural SOD at different temperatures. **f** Comparison of SOD activity between CuZnHis(L) and natural SOD at different pH. In Fig. 5a–f, data are presented as mean ± SD ($n = 3$).

assemblies is mainly attributed to the difference in specific surface area and, therefore, the number of exposed catalytic sites. Due to the larger size, the specific surface area of CuHis(L) assemblies is estimated as 6.2 $m^2/g$, which is only 37.3% of that of smaller CuZnHis(L) assemblies (Fig. S20). Correspondingly, the specific activity of CuHis(L) assemblies is 38.8% of that of CuZnHis(L) assemblies. Considering the specific surface area, their exposed catalytic sites and SOD activities are almost at the same level. Meanwhile, the small amount of $Zn^{2+}$ present in CuZnHis(L) assemblies form tetra-coordinated structure with N/O atoms (Fig. S21, Table S3), which has limited contribution on SOD activity. Furthermore, the specific surface area of CuZnHis(L) assemblies is also not so high, which is 16.6 $m^2/g$ (Fig. S20b), so the inner Cu sites are suppressed in participating catalytic reaction. It implies that the activity of a single Cu catalytic site should reach a very high level.

The SOD activity of CuZnHis(L) assembles is time- and concentration-dependent (Fig. 5c), but not affected by solvents. Besides water, the assemblies still maintain good $O_2^{\cdot-}$ scavenging ability in ethanol, isopropyl alcohol, acetonitrile, and DMF (Fig. 5d). Moreover, by normalizing the $O_2^{\cdot-}$ scavenging ability of natural SOD and CuZnHis(L) assemblies, the influence of temperature and pH on SOD activity are studied. Natural SOD and the assemblies do not show significant change in the activity in the temperature range of 5–35 °C. However, at 80 °C, the activity of natural SOD begins to decline, due to the conformational change and inactivation of natural enzyme. In comparison, the activity of CuZnHis(L) assemblies increases rather than decreases, because the catalytic reaction is accelerated at elevated temperature (Fig. 5e). In the pH range of physiological environment, both natural SOD and the assemblies show good stability, and the SOD activity is minimally affected (Fig. 5f). Apart from the temperature and pH stability, CuZnHis(L) assemblies also demonstrate good catalytic specificity. The existing artificial SODs generally face the common problems of nanoenzymes, that is, the active sites are exposed on the surface and prone to bind to the substrates, resulting in poor catalytic specificity. For example, while having SOD activity, artificial SODs usually exhibit high catalase (CAT) activity. Because CuZnHis(L) assemblies simulate the Cu catalytic sites of natural SOD accurately, they show low CAT activity and good catalytic specificity (Fig. S22). In addition, the $O_2^{\cdot-}$ scavenging ability of CuZnHis(D) is very close to CuZnHis(L), with an IC50 value of 0.137 μg/mL and a specific activity of 36500 Unit/mg, indicating that the chiral difference does not influence the SOD activity (Fig. 5a).

The high SOD activity endows CuZnHis assemblies with a good anti-inflammatory effect in vitro. CCK-8 tests show that the assemblies cause little damage to fibroblast cell L929 and rat periodontal ligament stem cell RPDLSC. The relative cell survival is still over 90% at the concentration of 200 μg/mL (Figs. S23, S24). The hemolysis test indicates that after co-incubation of red blood cells (RBCs) with the assemblies, the hemolysis rate is not significantly different from that of the negative control (Fig. S25). This reveals that the assemblies do not cause breakage and dissolution of RBCs, showing good biocompatibility. Reliable biosafety and biocompatibility stem from the structural stability of the assemblies. TEM observation indicates that the assemblies can enter RAW264.7 cells and maintain the original morphology (Fig. S26). The cell entry pathways of the assemblies are confirmed by inhibitor investigations. As shown in Fig. S27, the co-incubation with EIPA (macropinocytosis inhibitor), chlorpromazine (clathrin-mediated endocytosis inhibitor), and nystatin (caveolin-mediated endocytosis inhibitor) significantly reverses the cellular uptake of assemblies, suggesting that the entry pathways include macropinocytosis, clathrin-mediated endocytosis, and caveolin-mediated endocytosis. Based on the good biosafety and

biocompatibility, the effect of CuZnHis assemblies on the expression of inflammatory factors in macrophages is used to evaluate the anti-inflammatory performance. Inflammatory factors are mainly produced by immune cells, including both pro-inflammatory factors and anti-inflammatory factors. The former promotes the occurrence of inflammation or enhances the inflammatory reaction process. The latter reduces or even terminates the inflammatory response. In our work, the studies on the expression of inflammatory factors are carried out at three levels. The first is the determination of major cytokines, where qRT-PCR is used to detect the expression of related genes in RAW264.7 cells. CuZnHis assemblies significantly downregulate the expression of pro-inflammatory factors related genes (IL-1β and TNF-α), and upregulate the expression of anti-inflammatory factors related genes (IL-10 and TGF-β) (Fig. 6a). The second is the determination of relevant markers located on the membrane of RAW264.7 cells. As revealed by immunofluorescence staining, the expression of M1-type polarization marker CD86 in CuZnHis(L) and CuZnHis(D) groups is significantly decreased (Fig. 6b, c), and the expression of M2-type polarization marker CD206 is significantly increased (Fig. 6d, e). The third is the determination of relevant markers in the cytoplasm of RAW264.7 cells. Flow cytometry shows that CuZnHis assemblies significantly reduce the percentage of iNOS positive macrophages (Fig. 6f), but increase the percentage of Arg-1 positive macrophages (Fig. 6g). Further quantitative and statistical analysis more intuitively demonstrates the inhibition of iNOS expression and the promotion of Arg-1 expression by CuZnHis assemblies (Fig. S28). The aforementioned results indicate that CuZnHis assemblies can affect the phenotypes and functions of macrophages. The decreased expression of pro-inflammatory factors, including IL-1β, TNF-α, CD86, and iNOS, and the increased expression of anti-inflammatory factors, including IL-10, TGF-β, CD206, and Arg-1, clearly reflect the anti-inflammation of CuZnHis assemblies, which have the potential to treat oxidative stress-related diseases. It should be noted that the expression of pro-inflammatory factors in the CuZnHis(D) group is lower than that in the CuZnHis(L) group, and the expression of anti-inflammatory factors is opposite. This means that the CuZnHis(D) assemblies with D-type structure possess better anti-inflammatory effect than CuZnHis(L), though their SOD activity is similar. The differences in anti-inflammatory properties between CuZnHis(L) and CuZnHis(D) assemblies are mainly attributed to the influence of chirality on cells, with the primary reason being the reduction in immunogenicity caused by the "stealth-like" effect of the D-type structure[52,53]. Almost all the proteins in living organisms are composed of L-type amino-acids, but the spatial conformation of D-type structure does not match the natural receptors, which can effectively avoid being recognized by immune system, thereby avoiding the activation of pro-inflammatory signaling pathways[54,55]. The influence of chirality is further reflected in the ability to resist oxidative stress injury. The damage caused by ROS to cells and organisms can be indirectly reflected by the level of malondialdehyde (MDA). Compared with CuZnHis(L), CuZnHis(D) assemblies have stronger inhibitory effect on lipid peroxidation reactions, manifested as lower intracellular MDA level and stronger ability to resist oxidative stress injury (Fig. S29). CuZnHis(D) assemblies can promote the decrease in the expression of pro-inflammatory factors and the increase in the expression of anti-inflammatory factors more obviously[56,57]. The influence of chirality is also reflected in the antioxidant capacity. Glutathione (GSH) is the most abundant low-molecular-weight antioxidant in mammalian cells, and the consumption of GSH is a key factor in activating cellular autonomic inflammation[58]. Compared with CuZnHis(L), CuZnHis(D) assemblies prevent the decrease of intracellular GSH levels more obviously, show stronger antioxidant capacity, and alleviate the inflammatory response by reducing the expression of pro-inflammatory factors (Fig. S30).

As a proof of concept in treating oxidative stress-related diseases, CuZnHis assemblies remarkably inhibit the periodontitis in male animal models. The immune response triggered by periodontal tissue inflammation leads to the release of a large number of active substances, exacerbating the imbalance of the antioxidant system and tissue damage. Therefore, periodontitis is a representative disease related to oxidative stress[59,60]. For the established male animal models (Fig. 7a), severe inflammation occurs in the upper second molar of rats, and the gums are seriously red and swollen, forming deep periodontal pockets and large area absorption of alveolar bone. During the treatment, rats are administered with CuZnHis assemblies once every two weeks for a total of two times. The reason for choosing this time interval is that CuZnHis assemblies can maintain structural stability and functional stability within two weeks. After incubation in simulated body fluid and serum for two weeks, the morphology of CuZnHis(L) assemblies is still maintained (Figs. S31, S32). The coordination structure of CuZnHis(L) assemblies is also difficult to damage. After two weeks' incubation in simulated body fluid, the released $Cu^{2+}$ is only 4%. Most importantly, the SOD activity of CuZnHis(L) assemblies keeps as high as 31600 Unit/mg after two weeks' storage, only showing a decline of 16.6% (Fig. S33).

After the complete treatment cycle, Micro-CT, H&E and immunofluorescent staining data of the rat maxilla are used to evaluate the therapeutic effect. The Micro-CT scan and subsequent 3D reconstruction results show that the alveolar ridge height is greatly reduced in the control group, and even the root bifurcation is visible (Fig. 7b). Quantitative analysis shows that the distance from the cementoenamel junction (CEJ) to the alveolar bone crest (ABC) (CEJ-ABC) is 0.61, 0.70 and 0.66 mm at distal, median and mesial positions, respectively (Fig. S34). After the injection of CuZnHis assemblies into periodontal pocket, the periodontal inflammation is greatly inhibited. Intuitively, the CEJ-ABC values are 0.28, 0.33, and 0.49 mm in CuZnHis(L) group, and for CuZnHis(D) group, they are 0.27, 0.31, and 0.37 mm, which are about 56% and 48% of those in the control group (Fig. S34). The healing of periodontal tissues is also reflected in H&E staining. In the control group, a large number of inflammatory cells (mark with arrows) are infiltrated in the periodontal tissues, and the arrangement of collagen fibers (mark with dotted lines) is disordered, and edema and degeneration occur. After the treatment, the inflammatory cell infiltration in periodontal tissues is reduced and the collagen fibers are arranged in an orderly manner, showing a good curative effect (Fig. 7c). Immunofluorescent staining of periodontal tissues demonstrate that CuZnHis treatment significantly reduces the expression of IL-1β and TNF-α (Fig. 7d), and the downregulation of pro-inflammatory factors also demonstrates the ability of CuZnHis assemblies for treating inflammatory diseases. Similar to in vitro experiments, the difference in anti-inflammation caused by chiral difference is also observed in vivo. In the determination of periodontal tissues, CuZnHis(D) assemblies better increase the SOD level (Fig. S35), reduce the MDA level (Fig. S36), and increase the GSH level (Fig. S37), showing stronger capacity in antioxidant, which highlights CuZnHis(D) assemblies as better anti-inflammatory candidates.

The SOD activity of CuZnHis assemblies is compared with MnTMPyP and Tempol, two drugs in existing antioxidant therapies. After determination, the SOD activities of MnTMPyP and Tempol are 6200 Unit/mg and 32 Unit/mg, respectively (Figs. S38, S39), which are only 17% and 1‰ of the CuZnHis assemblies. This indicates the superior performance of CuZnHis assemblies. After the treatments, biosafety is systematically evaluated. Compared with the healthy rats of the same age, CuZnHis injection does not cause toxic side effects. The liver function (Fig. S40), kidney function (Fig. S41), and ion detection (Fig. S42) of the rats in the treatment groups are all normal. In addition, H&E staining of major organs in the treatment groups also shows normal histological morphology (Fig. S43). The pharmacokinetic behavior of CuZnHis(L) assemblies after administration via the tail vein is also examined. The blood circulation half-life of the assemblies is $0.88 \pm 0.03$ h, and the blood concentration decreases rapidly

https://doi.org/10.1038/s41467-025-65074-7

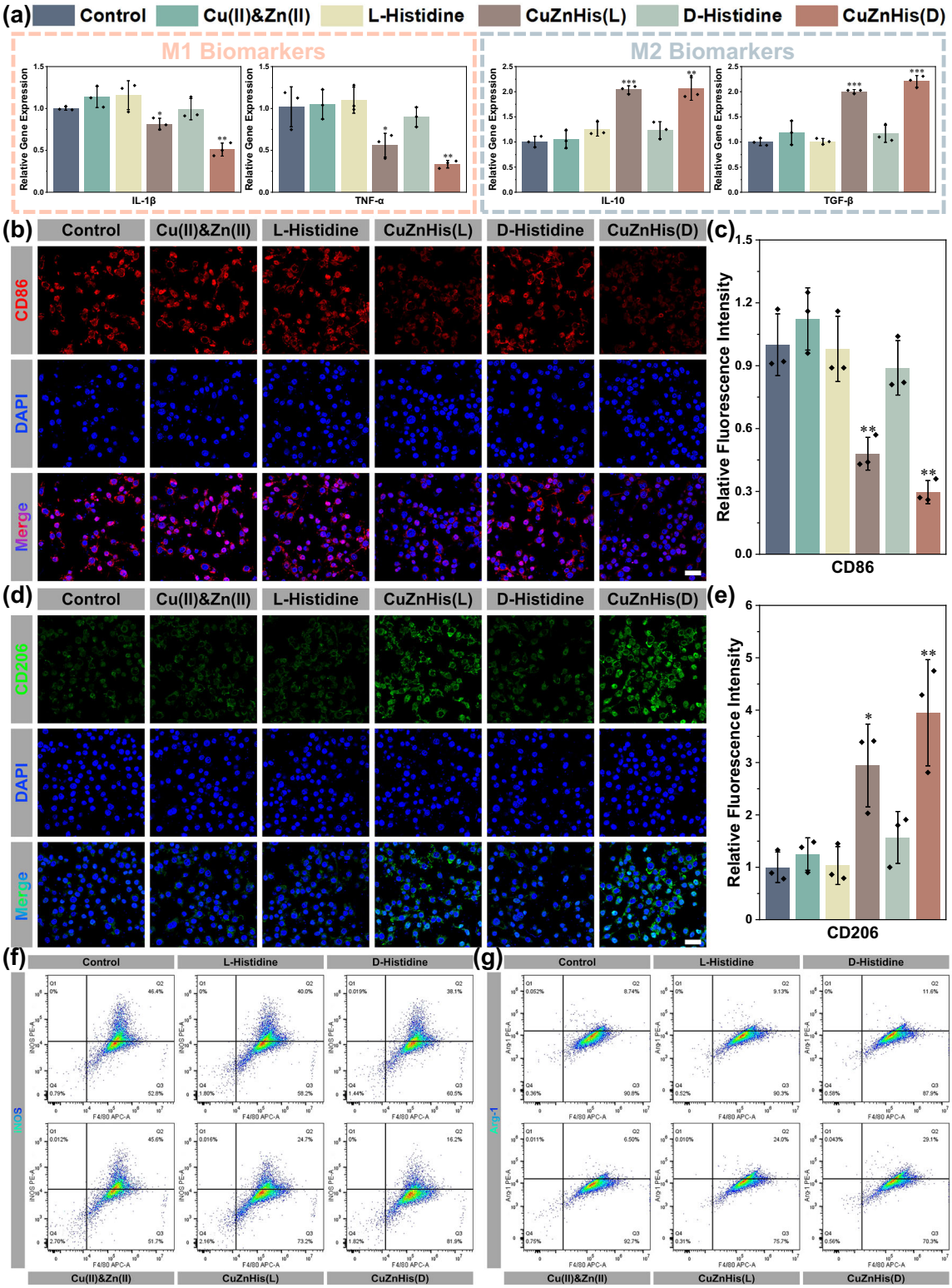


**Fig. 6 | Effect of CuZnHis assemblies on the expression of inflammatory factors in macrophages. a** The relative mRNA expression tested by qRT-PCR of pro-inflammatory factors related genes (IL-1β and TNF-α) and anti-inflammatory factors related genes (IL-10 and TGF-β) in lipopolysaccharide (LPS)-induced RAW264.7 cells after different treatments. Immunofluorescent staining (**b**) and quantitative analysis of fluorescence intensity (**c**) of CD86 in LPS-induced RAW264.7 cells after different treatments. Immunofluorescent staining (**d**) and quantitative analysis of fluorescence intensity (**e**) of CD206 in LPS-induced RAW264.7 cells after different treatments. The scale bar is 50 μm. The expression of iNOS (**f**) and Arg-1 (**g**) in LPS-induced RAW264.7 cells after different treatments measured by flow cytometry, the gate strategies were shown in Source Data. In Fig. 6a–e, data are presented as mean ± SD ($n = 3$), and $^{*}p < 0.05$, $^{**}p < 0.01$, $^{***}p < 0.001$ versus the Control group. Statistical significance was calculated via Student's t-test.

https://doi.org/10.1038/s41467-025-65074-7

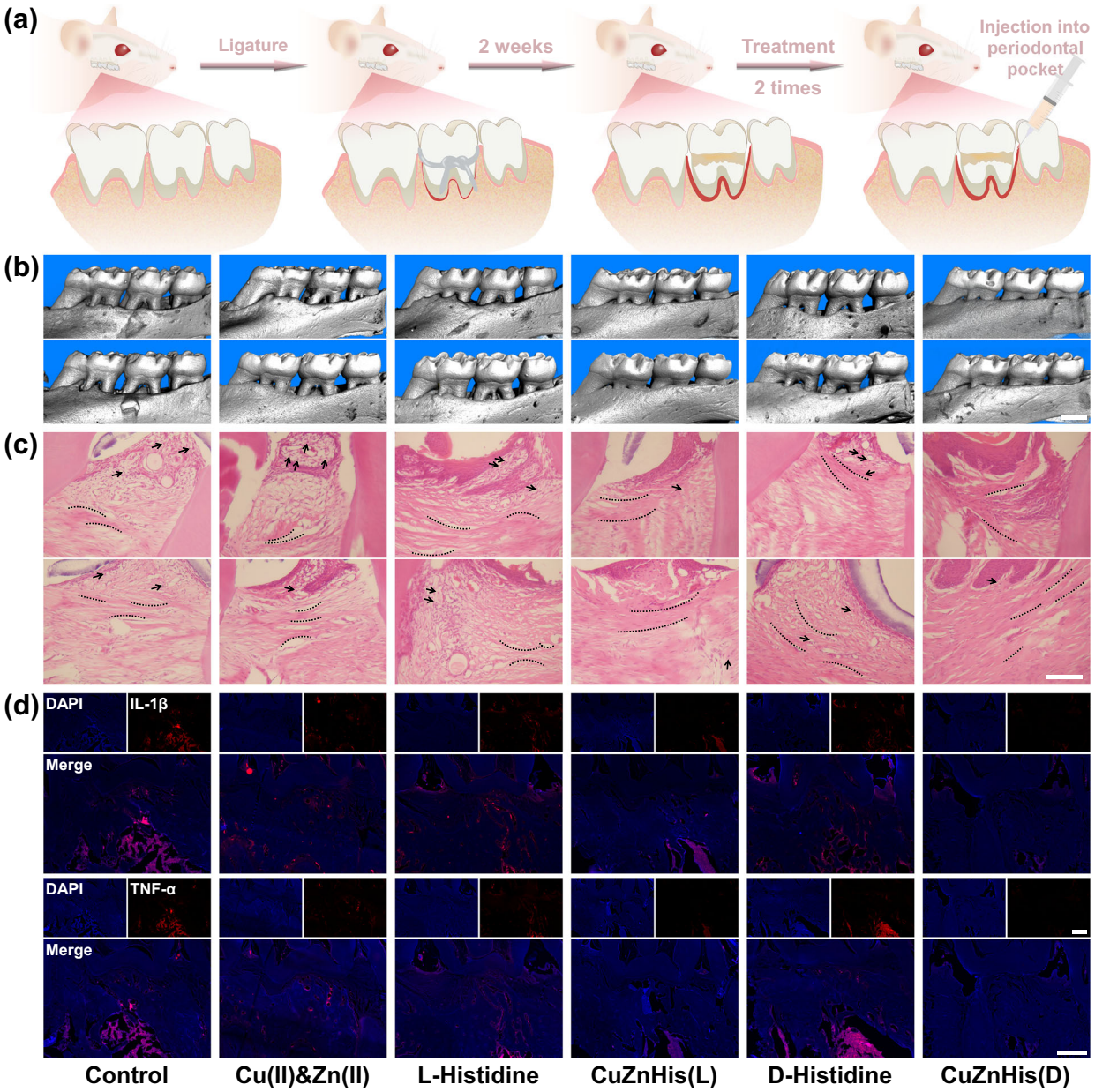


**Fig. 7 | Therapeutic effect of CuZnHis assemblies on oxidative stress-related diseases. a** Schematic illustration of the operations involved in animal experiments. **b** Micro-CT images of the maxilla of rats after different treatments. The scale bar is 1 mm. **c** H&E stained images of the maxillary slices of rats after different treatments. Inflammatory cell infiltration is indicated by arrows, and the arrangement direction of collagen fibers is indicated by dotted lines ($n = 3$). The scale bar is 200 μm. **d** Immunofluorescent staining of pro-inflammatory factors (IL-1β and TNF-α) in the maxillary slices of rats after different treatments ($n = 3$). The scale bar is 500 μm.

(Fig. S44). The accumulation of the assemblies in major organs decreases over time, which is basically metabolized after 7 days, avoiding the risk of long-term retention (Fig. S45). The reliable biosafety of CuZnHis assemblies indicates the prospect in the treatment of oxidative stress-related diseases. It should be mentioned that there are still deficiencies in our work. For instance, the focus is mainly on the optimization of catalytic sites and the preparation of assemblies without delving deeply into the in vivo metabolic and excretory behaviors of assemblies, and the importance of bacterial pathogens in the treatment of periodontitis. These will also be the key issues that need to be addressed in the future work. Besides, we are also constantly exploring the possible combinations of other metal ions and amino-acid to develop artificial SODs with higher performance and further expand the applications against oxidative stress-related disease, such as ischemia-reperfusion injury and ulcerative enteritis.

In summary, inspired by the $Cu^{2+}$/histidine residue coordination in natural Cu-Zn-SOD, an optimized Cu catalytic site is proposed for enhancing the activity of artificial SOD. Theoretical calculation result indicates that the tetrahedral coordination of $Cu^{2+}$ with one amino, one carboxyl and two imidazolyls is superior in terms of both site stability and catalytic activity. Accordingly, the CuZnHis assemblies with optimized Cu catalytic site prepared by entropy-driven self-assembly method present a significantly enhanced SOD activity up to 37900 Unit/mg, which is at least 5.4 times higher than that of natural Cu-Zn-SOD. As a proof of concept in treating oxidative stress-related diseases, CuZnHis assemblies promote the polarization of macrophages from M1 to M2 phenotype and the expression of anti-inflammatory factors, thus effectively curing periodontitis in male animal models. This work demonstrates a state-of-the-art design of artificial SOD by optimizing the catalytic

sites of natural SOD, which provides efficient candidates for the treatment of oxidative stress-related diseases.

## Methods

### Experimental materials

L-histidine (≥99%), sodium hydroxide (NaOH, 96%), copper nitrate trihydrate ($Cu(NO_3)_2{\cdot}3H_2O$, 99%), ethylene diamine tetraacetic acid disodium salt dihydrate (EDTA, 99%), urea (≥99.5%), sodium chloride (NaCl, 99.8%), and riboflavin sodium phosphate (93%) were purchased from Aladdin. Zinc nitrate hexahydrate ($Zn(NO_3)_2{\cdot}6H_2O$, AR) was purchased from Chengdu Kelong Chemical Co., Ltd. D-histidine (99%) and 5,5-dimethyl-1-pyrroline N-oxide (DMPO, 97%) were purchased from Shanghai Macklin Biochemical Technology Co., Ltd. Total superoxide dismutase assay kit with WST-8, lipid peroxidation MDA assay kit, GSH and GSSG assay kit, Triton X-100, DAPI, and bovine serum albumin (BSA) were purchased from Beyotime. Isopropyl alcohol (AR), and N, N-dimethylformamide (DMF, AR) were purchased from Tianjin Tiantai Chemical Co., Ltd. Acetone (AR) was purchased from Xilong Chemical Co., Ltd (Foshan). Ethanol absolute (SG), methanol (AR), and hydrochloric acid (AR) were purchased from Sinopharm Chemical Reagent Co., Ltd. PBS (0.01 M) was purchased from Biosharp. Tween-20 was purchased from BioFroxx. L929 mouse fibroblast cells, RAW264.7 cells, and cell counting kit-8 (CCK-8) were purchased from HyCyte. Rat periodontal ligament stem cells (RPDLSC) were purchased from Otwo Biotech. Cell culture flask and cell scraper were purchased from BaiDi Biotechnology Co., Ltd. (BDBIO). Confocal culture dish (1050001) was purchased from SAINING Biotechnology. DMEM culture medium, lipopolysaccharide (LPS), and hematoxylin-eosin (H&E) staining kit were purchased from Solarbio. Genomic PCR primer was purchased from Takara. CD16/32 antibody, IL-1β antibody, and TNF-α antibody were purchased from ProteinTech. CD86 antibody and CD206 antibody were purchased from Affinity. PE-labeled iNOS antibody, PE-labeled Arg-1 antibody, and APC-labeled F4/80 antibody were purchased from BioLegend. Wistar rats (6-week-old, male) were purchased from Liaoning Changsheng Biotechnology Co., Ltd. Isoflurane was purchased from RWD.

### Characterization

JEOL JEM-2100F transmission electron microscope (TEM) with an energy-dispersive X-ray spectroscopy (EDS) detector was used to collect TEM images and EDS elemental mapping images. Malvern NanoZS zetasizer was used to collect hydrated particle size and zeta potential. Palytical B.V. Empyrean X-ray diffractometer (XRD) was used to collect XRD pattern. Brucker Vertex 80 V Fourier transform infrared spectrometer (FTIR) was used to collect FTIR spectra. Horiba LabRAM HR Evolution Raman spectrometer was used to collect Raman spectra. Bruker Autoflex Speed MALDI-TOF was used to collect mass spectra. NETZSCH STA449F3 QMS403D Synchronous Thermal Analyzer coupled to mass spectrometry was used to collect thermal gravimetric analysis (TGA) and mass spectra of thermal decomposition products. VG Escalab MKII X-ray photoelectron spectrometer (XPS) was used to collect XPS spectra. Brucker Elexsys electron paramagnetic resonance (EPR) spectrometer was used to collect the EPR spectra. Agilent 725 inductively coupled plasma atomic emission spectroscopy (ICP-AES) was used to measure the concentrations of $Cu^{2+}$ and $Zn^{2+}$. The Mettler Toledo FE28 pH meter was used to measure the pH of the solution. The CMac Plus microplate reader was used to measure solution absorbance. The chemical state and configuration of Cu were investigated by X-ray absorption spectroscopy from Shanghai Synchrotron Radiation Facility (SSRF), BL14W beamline. The Applied Biosystems 7500 real-time fluorescence quantitative PCR instrument was used for qRT-PCR experiments. Yokogawa CSU-W1 confocal laser scanning microscope (CLSM) was used to collect CLSM images of cells. Beckman Coulter CytoFLEX was used for flow cytometry analysis. KEW KW-MZJ inhalation anesthesia system was used to anesthetoze rats. Scanco μCT50 Micro-CT was used to acquire CT images. The BDS400 microscope was used to acquire H&E and immunofluorescence-stained images.

### Preparation and characterization of CuZnHis assemblies

**Computational studies.** DFT calculations were carried out by the Gaussian 16 software[61]. The PBE0 functional was adopted for all calculations in combination with the D3BJ dispersion correction[62,63]. In geometry optimization and frequency calculations, the def2-TZVP basis set was used[64]. The singlet point energy calculations were performed with the same basis set combination. The solvation effects of water were considered during geometry optimizations using the SMD solvation model[64]. Although the PBE0-D3BJ/def2TZVP/SMD (water) calculation model still has limitations, for instance, the SMD implicit solvent model may have deficiencies when simulating the specific interactions between water molecules and solute Cu complexes, and the calculations carried out under standard temperature and pressure conditions also have limitations in simulating actual environmental factors, the optimized computational model is reliable and provides strong theoretical guidance for the optimization of catalytic sites.

**Preparation of CuZnHis assemblies.** 325.8 mg L-histidine, 50.4 mg NaOH, 253.68 mg $Cu(NO_3)_2{\cdot}3H_2O$, and 312.36 mg $Zn(NO_3)_2{\cdot}6H_2O$ were added to a mixed solution of 60 mL deionized water and 120 mL acetone. Then the solution was stirred at 50 °C for 12 h and CuZnHis(L) were prepared. The preparation method of CuZnHis(D) was the same as that of CuZnHis(L), except replacing L-histidine with D-histidine. After reaction, the product was centrifuged at 7200 × *g* for 10 min. All the supernatant was discarded and the precipitate was redissolved with deionized water. Then the centrifugation and redissolution operations were repeated for a total of 3 washes to remove unreacted reagents.

**XAFS data processing.** The XAFS data were analyzed following standard procedures with the Athena module of the IFEFFIT software package. The EXAFS spectra were derived through a two-step process, first, the post-edge background was subtracted from the total absorption, and second, normalizing was carried with respect to the edge-jump step. Fourier transform was applied to the χ(k) data, converting it into real (R) space with a Hanning window (dk = 1.0Å-1) to separate EXAFS contributions from distinct coordination shells. Quantitative structural parameters around central atoms were derived through least-squares curve parameters fitting performed in the ARTEMIS module of IFEFFIT software package[65,66].

**SOD activity of CuZnHis assemblies.** The total SOD activity detection kit (WST-8 method) was used to determine the SOD activity of the tested substances, and the corresponding test solution (WST-8/enzyme working liquid and reaction initiating working liquid) was prepared with PBS. WST-8 could react with $O_2^{\cdot-}$ generated by xanthine oxidase to produce water-soluble formazan dye, while substances with the catalytic ability of SOD could remove $O_2^{\cdot-}$ and inhibit the generation of formazan dye. The $O_2^{\cdot-}$ scavenging ability of natural SOD, CuZnHis(L), and CuZnHis(D) of different concentrations was measured and calculated by the difference in ΔAbs ($Abs_{450nm} - Abs_{630nm}$). Inhibition rate = $(\Delta Abs_{Control1} - \Delta Abs_{Sample}) / (\Delta Abs_{Control1} - \Delta Abs_{Control2}) \approx (\Delta Abs_{Control1} - \Delta Abs_{Sample}) / \Delta Abs_{Control1}$, and the SOD enzyme activity unit in the test sample = inhibition rate / (1 - inhibition rate) Unit. Then, the calculated result is divided by the mass of the substance to be measured in the solution to obtain the catalytic activity value in units/mg (When the inhibition rate in the above xanthine oxidase coupling reaction system is 50%, the SOD activity in the reaction system is defined as an enzyme activity Unit). In the experiment to verify the $O_2^{\cdot-}$ scavenging ability of CuZnHis by EPR, riboflavin sodium phosphate solution could produce $O_2^{\cdot-}$ when irradiated by UV

light with a wavelength of 365 nm, and DMPO was employed as a free radical trapping agent.

### Cell experiment

**Toxicity of CuZnHis assemblies.** The toxicity of CuZnHis assemblies to L929 cells and RPDLSC cells was determined by CCK-8 assay. L929 cells and RPDLSC cells were inoculated in 96-well plates at a density of 8000 cells per well and co-cultured with CuZnHis assemblies with the concentrations of 0, 25, 50, 100, 150, and 200 μg/mL for 24 h, respectively, then the optical density values at 450 nm were used to calculate the relative cell viability.

**Hemolysis test.** Rat 2% red blood cells were incubated with CuZnHis assemblies at the concentrations of 0, 100, 200, and 300 μg/mL for 1 h at 37 °C as experimental groups, with PBS as a negative control group, and with Triton X-100 as a positive control group. At the end of the incubation period, the samples were centrifuged at 2000 rpm for 10 min, and the absorbance value of the supernatant at 541 nm was measured to calculate the hemolysis rate. The hemolysis rate was calculated using the formula: $(A_{sample}-A_{negative}) / (A_{positive}-A_{negative}) * 100\%$.

**qRT-PCR.** RAW264.7 cells were inoculated into 6-well plates at a density of $2 \times 10^5$ cells/well, and LPS with a final concentration of 1 μg/mL was added 24 h later to induce an inflammatory environment for 24 h. The experiment was divided into 6 groups: Control group, Cu(II)&Zn(II) group, L-histidine group, CuZnHis(L) group, D-histidine group, and CuZnHis(D) group. The final concentrations of Cu and Zn ions in Cu(II)&Zn(II) group were 19.1 μg/mL and 0.6 μg/mL, respectively. The final concentrations of L-histidine and D-histidine were both 70.4 μg/mL. The final concentrations of CuZnHis(L) and CuZnHis(D) were both 100 μg/mL. After incubation for 24 h, RNA was extracted for qRT-PCR test to detect the gene expressions of IL-1β, TNF-α, IL-10 and TGF-β. The primers used in the qRT-PCR experiment were shown in Table S4.

**Immunofluorescent staining.** RAW264.7 cells were inoculated into confocal dishes at a density of $3 \times 10^4$ cells/well, and LPS with a final concentration of 1 μg/mL was added 24 h later to induce an inflammatory environment for 24 h. The experiment was also divided into 6 groups with the same dose concentration as the above experiment. After incubation for 24 h, the cells were fixed with paraformaldehyde (4%) for 15 min. Then, CD86 (1:500, Affinity) and CD206 (1:500, Affinity) primary antibodies were added and incubated at 4 °C overnight. The next day, fluorescent secondary antibody (1:1000) was added and incubated at 4 °C for 1h. After DAPI was added and incubated for 5 min, the cells were observed by CLSM.

**Flow cytometry.** RAW264.7 cells were inoculated into 6-well plates at a density of $2 \times 10^5$ cells/well, and LPS with a final concentration of 1 μg/mL was added 24 h later to induce an inflammatory environment for 24 h. The experiment was also divided into 6 groups with the same dose concentration as the above experiment. After incubation for 24 h, cells were collected and blocked for 30 min with 100 μL of BSA solution (3%) and CD16/32 antibody (1:100, ProteinTech). Then, PE-labeled iNOS antibody (1:200, BioLegend), PE-labeled Arg-1 antibody (1:200, BioLegend), and APC-labeled F4/80 antibody (1:200, BioLegend) were added and incubated for 30 min. After incubation, the supernatant was discarded by centrifugation. The collected cells were added with BSA solution (3%) and detected by flow cytometry. Each experiment was repeated three times.

### Animal experiment

**Establishment of periodontitis model in rats.** The animal experiments related to this work have been approved by the Animal Ethics Committee of the First Hospital of Jilin University. The feeding environment was 21–23 °C, 35–60% humidity, 12 h light-dark alternation. Thirty male Wistar rats of 6-week-old were selected for the experiment. After anesthetizing the rats with isoflurane inhalation, a wire ligation with a diameter of 0.25 mm was inserted through the distal proximal surface of the maxillary second molar of the rats, circumvented around the neck of the molar, and carried out through the mesial proximal surface of the molar. After ligature, keep about 2 mm and bend back to the gingiva to ensure that the wire ligation wire does not fall off. After 2 weeks, the wire ligation was removed, and the gums of the second molar were red and swollen, forming deep periodontal pockets, and the periodontitis model was successfully established.

**Treatment of periodontitis by CuZnHis assemblies.** Thirty rats were randomly divided into 6 groups, which were named Control group, Cu(II)&Zn(II) group, L-histidine group, CuZnHis(L) group, D-histidine group and CuZnHis(D) group, respectively. Then, according to the experimental group, the rats were administered once every 2 weeks into the periodontal pocket with a total of two times. Among them: Control group, 50 μL normal saline was injected into the periodontal pocket; Cu(II)&Zn(II) groups, 50 μL mixed solution with $Cu^{2+}$ concentration of 3.82 mg/mL and $Zn^{2+}$ concentration of 0.16 mg/mL was injected into the periodontal pocket; L-Histidine group and D-histidine group, 50 μL corresponding solution with the concentration of 14.08 mg/mL was injected into the periodontal pocket; CuZnHis(L) group and CuZnHis(D) group, 50 μL corresponding solution with the concentration of 20 mg/mL was injected into the periodontal pocket. The formation of deep periodontal pockets caused by periodontitis provides space for the administration of CuZnHis, and can effectively avoid the loss of drugs. After 4 weeks, the rats were euthanized, and the maxillae were dissected. After being fixed in 4% paraformaldehyde solution for 48 h, the samples were scanned, 3D reconstructed, and analyzed by Micro-CT. Then the samples were decalcified in EDTA solution for 4 weeks, and after sectioning, H&E staining were performed to evaluate inflammatory cell infiltration in periodontal tissue.

**Detection of inflammatory factor expression in periodontal tissue.** The maxillae of each group of rats obtained in the experiment was used for immunofluorescence staining to evaluate the expression of inflammatory factor. The primary antibodies were IL-1β (1:100, ProteinTech) and TNF-α (1:100, ProteinTech), and the incubation time was 12 h. For the fluorescent secondary antibody, the incubation time was 1 h. Under fluorescence microscopy, the cell nuclei are stained blue by DAPI and the target proteins appear red.

### Reporting summary

Further information on research design is available in the Nature Portfolio Reporting Summary linked to this article.

## Data availability

Data supporting the findings of this work are available within the paper and its Supplementary Information file. Source data are provided with this paper and the raw data are available upon request to the corresponding authors. Source data are provided with this paper.

## References

1. Cheng, F. et al. DJ-1 is dispensable for human stem cell homeostasis. *Protein Cell* **10**, 846–853 (2019).
2. Zhang, H. J. et al. Redox regulation and its emerging roles in cancer treatment. *Coord. Chem. Rev.* **475**, 214897 (2023).
3. Hassen, W. et al. On the redox profile of B- cell terminal differentiation and multiple myeloma: new insights and therapeutic opportunities. *Blood* **128**, 5644 (2016).
4. Chen, Y. et al. Metabolic reprogramming in memory CD4+T cells is associated with reactive oxygen induced immune cell dysfunction during aging. *Ann. Rheum. Dis.* **80**, 191 (2021).

5. Liu, W. L. et al. Integrated cascade nanozymes with antisenescence activities for atherosclerosis therapy. *Angew. Chem., Int. Ed.* **62**, 202304465 (2023).
6. Sczepanik, F. S. C. et al. Periodontitis is an inflammatory disease of oxidative stress: we should treat it that way. *Periodontol* **84**, 45–68 (2020).
7. Yang, B. W., Chen, Y. & Shi, J. L. Reactive oxygen species (ROS)-based nanomedicine. *Chem. Rev.* **119**, 4881–4985 (2019).
8. Wang, Z. Z. et al. Accelerated discovery of superoxide-dismutase nanozymes via high-throughput computational screening. *Nat. Commun.* **12**, 6866 (2021).
9. Li, Y. N., Yan, L., Kong, X., Chen, J. W. & Zhang, H. B. Cloning, expression, and characterization of a novel superoxide dismutase from deep-sea sea cucumber. *Int. J. Biol. Macromol.* **163**, 1875–1883 (2020).
10. Zhao, H. Q., Zhang, R. F., Yan, X. Y. & Fan, K. L. Superoxide dismutase nanozymes: an emerging star for anti-oxidation. *J. Mater. Chem. B* **9**, 6939–6957 (2021).
11. Azadmanesh, J., Lutz, W. E., Coates, L., Weiss, K. L. & Borgstahl, G. E. O. Direct detection of coupled proton and electron transfers in human manganese superoxide dismutase. *Nat. Commun.* **12**, 2079 (2021).
12. Johnson, F. & Giulivi, C. Superoxide dismutases and their impact upon human health. *Mol. Asp. Med.* **26**, 340–352 (2005).
13. Azadmanesh, J. & Borgstahl, G. E. O. A review of the catalytic mechanism of human manganese superoxide dismutase. *Antioxidants* **7**, 25 (2018).
14. Smirnov, V. V. & Roth, J. P. Mechanisms of electron transfer in catalysis by copper zinc superoxide dismutase. *J. Am. Chem. Soc.* **128**, 16424–16425 (2006).
15. Lintuluoto, M., Yamada, C. & Lintuluoto, J. M. QM/MM calculation of the enzyme catalytic cycle mechanism for copper- and zinc-containing superoxide dismutase. *J. Phys. Chem. B* **121**, 7235–7246 (2017).
16. Tainer, J. A., Getzoff, E. D., Richardsont, J. S. & Richardson, D. C. Structure and mechanism of copper, zinc superoxide dismutase. *Nature* **306**, 284–287 (1983).
17. Yamazaki, Y. & Takao, T. Metalation states versus enzyme activities of Cu, Zn-superoxide dismutase probed by electrospray ionization mass spectrometry. *Anal. Chem.* **80**, 8246–8252 (2008).
18. Manieri, T. M., Sensi, S. L., Squitti, R. & Cerchiaro, G. Structural effects of stabilization and complexation of a zinc-deficient superoxide dismutase. *Heliyon* **7**, e06100 (2021).
19. Kubota, S. & Yang, J. T. Bis[cyclo(histidylhistidine)]copper(II) complex that mimicks the active center of superoxide dismutase has its catalytic activity. *Proc. Natl Acad. Sci. USA* **81**, 3283–3286 (1984).
20. Azadmanesh, J. et al. Revealing the atomic and electronic mechanism of human manganese superoxide dismutase product inhibition. *Nat. Commun.* **15**, 5973 (2024).
21. Wang, D. J., Zhao, X. J., Vargek, M. & Spiro, T. G. Metal-bound histidine modes in UV resonance raman spectra of Cu, Zn superoxide dismutase. *J. Am. Chem. Soc.* **122**, 2193–2199 (2000).
22. Ellerby, L. M., Cabelli, D. E., Graden, J. A. & Valentine, J. S. Copper-zinc superoxide dismutase: why not pH-dependent? *J. Am. Chem. Soc.* **118**, 6556–6561 (1996).
23. Zhang, A. Y., Koone, J. C., Dashnaw, C. M., Zahler, C. T. & Shaw, B. F. Complete charge regulation by a redox enzyme upon single electron transfer. *Angew. Chem., Int. Ed.* **59**, 10989–10995 (2020).
24. Trist, B. G., Hilton, J. B., Hare, D. J., Crouch, P. J. & Double, K. L. Superoxide dismutase 1 in health and disease: how a frontline antioxidant becomes neurotoxic. *Angew. Chem., Int. Ed.* **60**, 9215–9246 (2021).
25. Duncan Lyngdoh, R. H., Schaefer, H. F. I. I. I. & King, R. B. Metal-metal (MM) bond distances and bond orders in binuclear metal complexes of the first row transition metals titanium through zinc. *Chem. Rev.* **118**, 11626–111706 (2018).
26. Jiang, S. C. et al. Additive-free $CO_2$ hydrogenation to pure formic acid solution via amine-modified Pd catalyst at room temperature. *Green. Chem.* **25**, 6025–6031 (2023).
27. Wang, J. Y. et al. Activation of MOF catalysts with low steric hindrance via undercoordination chemistry for efficient polysulfide conversion in lithium-sulfur battery. *Adv. Energy Mater.* **14**, 2402072 (2024).
28. Ciano, L., Davies, G. J., Tolman, W. B. & Walton, P. H. Bracing copper for the catalytic oxidation of C-H bonds. *Nat. Catal.* **1**, 571–577 (2018).
29. Wang, Z. F., Feng, S. S., Rovira, C. & Wang, B. J. How oxygen binding enhances long-range electron transfer: lessons from reduction of lytic polysaccharide monooxygenases by cellobiose dehydrogenase. *Angew. Chem., Int. Ed.* **60**, 2385–2392 (2021).
30. Du, X. S. et al. Molecular transformations of arsenic species in the flue gas of typical power plants: a density functional theory study. *Energy Fuels* **30**, 4209–4214 (2016).
31. Vannatta, P. E., Ramirez, D. A., Velarde, A. R., Ali, G. & Kieber-Emmons, M. T. Exceptionally high O-H bond dissociation free energy of a dicopper(II) μ-hydroxo complex and insights into the geometric and electronic structure origins thereof. *J. Am. Chem. Soc.* **142**, 16292–16312 (2020).
32. Yang, B. W. et al. In situ synthesis of natural antioxidase mimics for catalytic anti-inflammatory treatments: rheumatoid arthritis as an example. *J. Am. Chem. Soc.* **144**, 314–330 (2022).
33. Sigel, H. & McCormick, D. B. Some literature dealing with Cu(II)-L-histidine 1:2 complex in solution. *J. Am. Chem. Soc.* **93**, 2041–2044 (1971).
34. Leberman, R. & Rabin, B. R. Multiplicity of histidine-Cu(II) complexes. *Nature* **183**, 746–747 (1959).
35. Kotuniak, R. et al. Key intermediate species reveal the copper(II)-exchange pathway in biorelevant ATCUN/NTS complexes. *Angew. Chem. Int. Ed.* **59**, 11234–11239 (2020).
36. Xu, J. T. et al. Metal-coordinated supramolecular self-assemblies for cancer theranostics. *Adv. Sci.* **8**, 2101101 (2021).
37. Li, Y., Huang, F. H., Stang, P. J. & Yin, S. C. Supramolecular coordination complexes for synergistic cancer therapy. *Acc. Chem. Res.* **57**, 1174–1187 (2024).
38. Dashtestani, F., Ghourchian, H. & Najafi, A. Albumin coated copper-cysteine nanozyme for reducing oxidative stress induced during sperm cryopreservation. *Bioorg. Chem.* **80**, 621–630 (2018).
39. Yang, M., Jiang, W., Pan, Z. Q. & Zhou, H. Synthesis, characterization and SOD-like activity of histidine immobilized silica nanoparticles. *J. Inorg. Organomet. Polym. Mater.* **25**, 1289–1297 (2015).
40. Xia, X. M. et al. Construction of self-assembled nanogel as multienzyme mimics for bioresponsive tandem-catalysis imaging. *Sci. China Mater.* **64**, 3079–3086 (2021).
41. Zhang, Y. J. et al. Integrating Pt nanoparticles with carbon nanodots to achieve robust cascade superoxide dismutase-catalase nanozyme for antioxidant therapy. *Nano Today* **49**, 101768 (2023).
42. Gao, W. H. et al. Deciphering the catalytic mechanism of superoxide dismutase activity of carbon dot nanozyme. *Nat. Commun.* **14**, 160 (2023).
43. Lu, X. Y. et al. Single-atom catalysts-based catalytic ROS clearance for efficient psoriasis treatment and relapse prevention via restoring ESR1. *Nat. Commun.* **14**, 6767 (2023).
44. Li, G. M. et al. Dimensionality engineering of single-atom nanozyme for efficient peroxidase-mimicking. *J. Am. Chem. Soc.* **145**, 16835–16842 (2023).
45. Meng, X. Q. et al. Ultrasmall metal alloy nanozymes mimicking neutrophil enzymatic cascades for tumor catalytic therapy. *Nat. Commun.* **15**, 1626 (2024).
46. Guo, Z. J., Hong, J. J., Song, N. N. & Liang, M. M. Single-atom nanozymes: from precisely engineering to extensive applications. *Acc. Mater. Res.* **5**, 347–357 (2024).

47. Liang, M. M. & Yan, X. Y. Nanozymes: from new concepts, mechanisms, and standards to applications. *Acc. Chem. Res.* **52**, 2190–2200 (2019).
48. Zhang, X. Y. et al. The entropy-controlled strategy in self-assembling systems. *Chem. Soc. Rev.* **52**, 6806–6837 (2023).
49. Ji, H. M. et al. High-entropy solvent design enabling a universal electrolyte with a low freezing point for low-temperature aqueous batteries. *Chem. Commun.* **59**, 8715–8718 (2023).
50. Wu, H. et al. Citric acid-assisted ultrasmall $CeO_2$ nanoparticles for efficient photocatalytic degradation of glyphosate. *Chem. Eng. J.* **425**, 130640 (2021).
51. Liu, C. et al. Intrinsic strain-mediated ultrathin ceria nanoantioxidant. *J. Am. Chem. Soc.* **145**, 19086–19097 (2023).
52. He, Y. D. et al. Biomimetic chiral nanotopography for manipulating immunological response. *Adv. Funct. Mater.* **34**, 2313157 (2024).
53. Jiang, W. et al. Chiral metal-organic frameworks incorporating nanozymes as neuroinflammation inhibitors for managing Parkinson's disease. *Nat. Commun.* **14**, 8137 (2023).
54. Zhang, X. Y., An, Z. H., An, J. & Tian, X. Bioinspired chiral nanozymes: synthesis strategies, classification, biological effects and biomedical applications. *Coord. Chem. Rev.* **502**, 215601 (2024).
55. Zhang, Y. et al. Chirality-dependent reprogramming of macrophages by chiral nanozymes. *Angew. Chem. Int. Ed.* **62**, e202307076 (2023).
56. Huang, S. G. et al. Anti irradiation nanoparticles shelter immune organ from radio-damage via preventing the IKK/IκB/NF-κB activation. *Mol. Cancer* **23**, 234 (2024).
57. Yang, T. et al. Dietary nitrate attenuates renal ischemia-reperfusion injuries by modulation of immune responses and reduction of oxidative stress. *Redox Biol.* **13**, 320–330 (2017).
58. He, Z. S. et al. Resolvin D1 delivery to lesional macrophages using antioxidative black phosphorus nanosheets for atherosclerosis treatment. *Nat. Nanotechnol.* **19**, 1386–1398 (2024).
59. Li, T. C. et al. Triple-combination therapy with a multifunctional yolk-shell nanozyme Au@$CeO_2$ loaded with dimethyl fumarate for periodontitis. *Adv. Sci.* **12**, 2413891 (2025).
60. Zhu, C. et al. Manganese dioxide coupled metal-organic framework as mitophagy regulator alleviates periodontitis through SIRT1-FOXO3-BNIP3 signaling axis. *Biomaterials* **319**, 123179 (2025).
61. Frisch, M. et al. Gaussian 09, revision D. 01. Gaussian, Inc., Wallingford CT, 2009.
62. Adamo, C. & Barone, V. Toward reliable density functional methods without adjustable parameters: the PBE0 model. *J. Chem. Phys.* **110**, 6158–6170 (1999).
63. Weigend, F. & Ahlrichs, R. Balanced basis sets of split valence, triple zeta valence and quadruple zeta valence quality for H to Rn: design and assessment of accuracy. *Phys. Chem. Chem. Phys.* **7**, 3297–3305 (2005).
64. Marenich, A. V., Cramer, C. J. & Truhlar, D. G. Universal solvation model based on solute electron density and on a continuum model of the solvent defined by the bulk dielectric constant and atomic surface tensions. *J. Phys. Chem. B* **113**, 6378–6396 (2009).
65. Ravel, B. & Newville, M. ATHENA, ARTEMIS, HEPHAESTUS: Data analysis for X-ray absorption spectroscopy using IFEFFIT. *J. Synchrotron Radiat.* **12**, 537–541 (2005).
66. Zabinsky, S. I., Rehr, J. J., Ankudinov, A., Albers, R. C. & Eller, M. J. Multiple-scattering calculations of X-ray-absorption spectra. *Phys. Rev. B* **52**, 2995–3009 (1995).


## Acknowledgements

This work was supported by the National Natural Science Foundation of China (52303085), the Science and Technology Development Program of Jilin Province (Grant Number SKL202302001), and a Special Project from MOST of China. The authors thank the Electron Microscopy Platform of the First Hospital of Jilin University for their technical support in biological sample preparation and operation.

## Author contributions

H.Zha. and S.L. proposed the project and designed the experiments. H.J. and X.Z. performed the synthetic experiments and biological experiments. M.Z. and Y.C. participated in biological experiments. H.Zhe. participated in synthetic experiments. D.Y. performed the theoretical calculation. H.Zha., S.L., and H.J. co-wrote the paper. All authors have given approval to the final version of the manuscript.

## Competing interests

The authors declare no competing interests.

## Additional information

**Supplementary information** The online version contains supplementary material available at https://doi.org/10.1038/s41467-025-65074-7.

**Correspondence** and requests for materials should be addressed to Shuwei Liu or Hao Zhang.

**Peer review information** *Nature Communications* thanks Kelong Fan, Minmin Liang, and the other, anonymous, reviewer for their contribution to the peer review of this work. A peer review file is available.